


Internal circulation and mixing within tight-squeezing deformable dropletsJacob R. Gissinger ^{*}, Alexander Z. Zinchenko, and Robert H. Davis*Department of Chemical and Biological Engineering, University of Colorado, Boulder, Colorado 80309-0596, USA*

(Received 14 July 2020; revised 2 February 2021; accepted 8 April 2021; published 28 April 2021)

The internal flow and mixing properties inside deformable droplets, after reaching the steady state within two types of passive droplet traps, are visualized and analyzed as dynamical systems. The first droplet trap (constriction) is formed by three spheres arranged in an equilateral triangle, while the second consists of two parallel spherocylinders (capsules). The systems are assumed to be embedded in a uniform far-field flow at low Reynolds number, and the steady shapes and interfacial velocities on the drops are generated using the boundary-integral method. The internal velocity field is recovered by solving the internal Dirichlet problem, also via a desingularized boundary-integral method. Calculation of 2D streamlines within planes of symmetry reveals the internal equilibria of the flow. The type of each equilibrium is classified in 3D and their interactions probed using passive tracers and their Poincaré maps. For the two-capsule droplet, saddle points located on orthogonal symmetry planes influence the regular flow within the drop. For the three-sphere droplet, large regions of chaos are observed, embedded with simple periodic orbits. Flow is visualized via passive dyes, using material lines and surfaces. In 2D, solely the interface between two passive interior fluids is advected using an adaptive number of linked tracer particles. The reduction in dimension decreases the number of required tracer points, and also resolves arbitrarily thin filaments, in contrast to backward cell-mapping methods. In 3D, the advection of a material surface, bounded by the droplet interface, is enabled using an adaptive mesh scheme. Off-lattice 3D contour advection allows for highly resolved visualizations of the internal flow and quantification of the associated degree of mixing. Analysis of the time-dependent growth of material surfaces and 3D mixing numbers suggests the three-sphere droplet exhibits superior mixing properties compared to the two-capsule droplet.

DOI: [10.1103/PhysRevE.103.043106](https://doi.org/10.1103/PhysRevE.103.043106)**I. INTRODUCTION**

As droplets are used for increasingly precise tasks, such as microreactors in microfluidic systems, it has become more important to understand how the confinement geometry affects their internal flow. For example, certain microfluidic designs include arrays of static droplet traps to enable reactive mixing for a set residence time before releasing the drops by reversing the flow direction [1]. Interesting optimization questions arise: Do certain droplet-trap shapes increase the degree of mixing? What is the effect of introducing asymmetry into the droplet trap? Computational tools have the potential to screen a large number of geometries to help answer these questions, both to estimate the amount of mixing and for precise determination of properties of the internal velocity field, such as the topology and complexity of the flow.

Mixing is notoriously slow in the low-Reynolds-number (Stokes) regime, at which most microfluidic devices operate, but chaotic advection has been shown to greatly increase mixing [2]. Aref *et al.* [3] provided a recent comprehensive review of chaotic advection, including methods to characterize such a flow, quality-of-mixing metrics, and its application in flows from microfluidics to oceanographic scales [3]. Subjecting a flow to time-dependent perturbations provides a straightforward way to introduce chaos, as traditionally demonstrated by the blinking vortex model [4,5]. However, chaos has also

been demonstrated to occur in steady flows, such as the ABC flow originally reported by Arnold [6,7], and the characterization of steady chaotic advection remains an active topic of research. For example, the Lagrangian flow topology in cavity flows was recently shown to react to nonlinear effects according to universal mechanisms within domains of a given symmetry [8]. An important feature of such flows is the Kolmogorov-Arnold-Moser (KAM) torus; KAM tori that are stable to perturbations define persistent barriers within a flow. In the Stokes regime, Bajer and Moffatt [9] demonstrated a quadratic flow within a spherical domain that exhibits stretch-twist-fold chaotic dynamics. Subsequently, Stone *et al.* [10] provided a simpler example of chaos inside a spherical droplet subject to linear Stokes flows. Chaos has since been demonstrated in many other systems relevant to microfluidics, such as channel and emulsion flows, and chaotic advection is critical to the effectiveness of micromixers [11]. Properties of these flows can be quantified within the mathematical framework of dynamical systems. The traditional tool used to visualize the flow of these systems is the Poincaré section, which is the intersection of a trajectory with a plane. More recently, other numerical tools (e.g., topological structure) as well as additional measures from chaos theory (e.g., Lyapunov exponents, see Boffetta *et al.* [12] and Wiggins and Ottino [13]) have become prevalent. The numerical determination of topological structures, such as equilibria (stagnation points) and periodic orbits, and the relationships between them, can be derived from discrete Morse theory [14] or by analysis of the gradient field [15].

^{*}jacob.r.gissinger@gmail.com

More direct dynamic visualizations of mixing are important both for experimental and numerical studies. Microfluidic drops can be mixed during flow by serpentine channels [16,17] or by introducing irregular obstructions into the channel [18]. Internal flows are often visualized by the passive advection of dye, e.g., initially filling one-half of the drop [19,20], or by particle image velocimetry [21,22]. More advanced techniques allow for fully 3D tracking of tracer particles, which enables the delineation of completely new types of coherent structures and more direct comparison with simulation [23]. Visualizations of numerical simulations borrowed these ideas directly: passive tracers are used to plot 3D trajectories and map out Poincaré sections [24] or blobs of passive dye are simulated by advecting material volumes [25]. An issue arises when these material volumes are composed of many passive particles imagined to have finite size. Although the blob initially appears contiguous, eventually the constituent particles will separate enough that the blob no longer appears connected, even when the Hamiltonian nature of the flow technically prevents such a topological transformation. Even though, given sufficient tracer particles, this simple method often provides an adequate picture of the flow and can even mirror experimental images due to the breakup of thin filaments under capillary instability, more exacting methods are required to maintain high resolution at longer times [26]. For example, the backward Poincaré cell-map method utilizes fixed cells instead of mobile tracers and results in considerably less noise during material advection when applied to chaotic systems [27].

Arbitrary resolution can be achieved by explicitly tracking the evolving interface, e.g., with a line or surface of connected tracers. This concept seems to have been introduced independently in application to inviscid flows, where it is known as contour advection [28–30], and for creeping flow in application to a driven cavity, where it is known as a material surface [31,32]. A potentially significant drawback, even with modern computing power, is that material surfaces in chaotic flow grow exponentially [33,34]. On the other hand, this hallmark of chaos can therefore be arbitrarily resolved and readily computed using the material surface method. For example, the rate of growth of material lines and surfaces is related to useful measures such as the topological entropy [35,36]. Retaining connectivity between tracers can also reveal topological properties of the flow in a robust manner [37,38]. From a numerical standpoint, the local resolution of a material surface can be maintained by simply inserting an additional tracer between nodes that exceed a prescribed separation or by more advanced methods that account for curvature of the surface or allow for splitting and reconnection (surgery) [39,40].

Advection of a passive dye, or material blob, provides quantitative information about mixing efficiency when a measure for the degree of mixing is defined. Many such measures to quantify mixing have been proposed. Metrics include thickness of the striated layers of the dye or fractal dimension of its interface [2], stretching statistics or particle spread [41,42], or the average distance between each point in one fluid dye to the other [43]. Perhaps this last metric is particularly suited for simple analysis of either experimental or numerical images that can be converted into two-color images, where pixels provide a natural discretization of the field. In all cases, the

goal is to convert a time series of flow snapshots (typically assumed to be nondiffusive) into a scalar that is indicative of how well mixed the fluid is, i.e., how quickly diffusion can result in a completely homogeneous fluid. Finn *et al.* [44] provided a direct comparison between many classes of mixing metrics and demonstrated that they are not always well correlated, which emphasizes that determining a suitable measure often requires a case-by-case evaluation.

In the present paper, we use many of the above tools to provide a comprehensive picture of the internal flow and mixing in deformable droplets trapped in two simple types of constrictions, one comprised of solid capsules with twofold symmetry, and the other one of solid spheres with threefold symmetry. The configurations of these constrictions are provided in Sec. II. The desingularized boundary-integral formulation used to solve the internal Dirichlet problem and recover the internal velocity field is presented in Sec. III. Numerical and technical details regarding how passive tracers and material lines and surfaces were advected and visualized are given in Sec. IV. Particular technical challenges were presented when the material surface, advected in three dimensions, was assumed to be bounded by an arbitrary, dynamic loop on the droplet interface. The explicit 3D advection and visualization techniques presented herein offer high-resolution qualitative and quantitative insight into the internal dynamics of these confined systems. In Sec. V, the internal flow within a drop trapped in the two types of constrictions is analyzed from a dynamical systems standpoint and visualized using passive tracers and dyes, and the relative strength of each constriction as a passive droplet mixer is characterized. Concluding remarks are provided in Sec. VI.

II. PROBLEM FORMULATION

Consider a deformable droplet in Stokes flow that has entered a constriction composed of solid particles and become trapped indefinitely. The system properties (notably the capillary number) required for such an occurrence have been the subject of previous work, assuming that the droplet is neutrally buoyant, was initially spherical, and freely suspended in a uniform flow \mathbf{u}_∞ far away from the solid particles (and aiming at the constriction center), and both the drop and carrier fluids are Newtonian Stokes flows,

$$-\nabla p + \mu \nabla^2 \mathbf{u} = 0, \quad \nabla \cdot \mathbf{u} = 0, \quad (1)$$

where p is pressure and μ is viscosity. The solid particles are fixed in space [45,46], and the trapped state is generated by a long-time boundary-integral dynamical simulation, the ultimate interfacial fluid velocity \mathbf{u} on the drop surface being a part of the solution. Once this interfacial velocity is known, the flow inside the trapped drop can be recovered through the solution of an additional boundary-integral problem and happens to be non-trivial (see Sec. III for more detail). The analysis of this internal flow, its mixing, and topological properties is the major goal of the present paper.

Two simple constrictions with specific geometries are considered (leading to vastly different mixing behaviors), one composed of equisized spheres with threefold symmetry and another one made up of parallel capsules and having twofold symmetry. These systems are well-defined from a theoretical

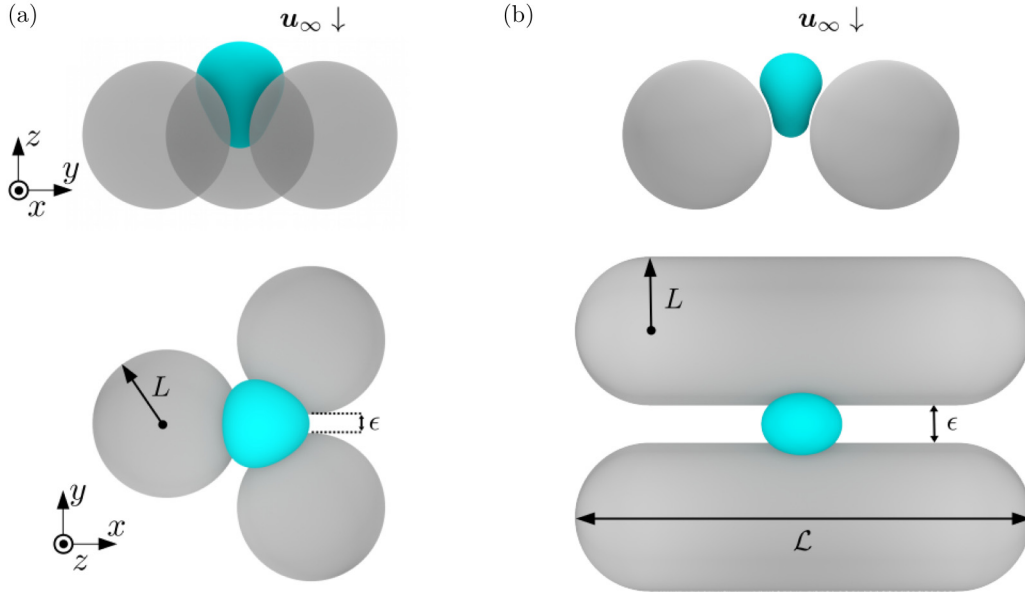


FIG. 1. Side and top views of two trapped-droplet systems embedded in a far-field flow (of uniform velocity \mathbf{u}_∞) and with characteristic length L . (a) A droplet ($\tilde{a} = 0.6$) trapped between three spheres ($\text{Ca} = 0.9$, $\lambda = 4$, $\epsilon = 0.25$). (b) A droplet ($\tilde{a} = 0.5$) trapped between two capsules ($\text{Ca} = 0.7$, $\lambda = 4$, $\epsilon = 0.5$, $\mathcal{L} = 6$).

standpoint, being completely described by nondimensional parameters and embedded in an infinite domain with uniform far-field flow, but result in a complex steady-state flow typical of passively trapped drops in microfluidics and porous media [1,47]. The characteristic length L of a system is the radius of the sphere or capsule, respectively, as shown in Fig. 1. The constriction gap ϵ (set to $0.25L$ for the three-sphere and to $0.5L$ for the two-capsule constriction) is defined as the minimum surface clearance between the solid particles. The capsule length \mathcal{L} for the two-capsule construction is $\mathcal{L} = 6L$. The nondeformed drop radius \tilde{a} is chosen to be $0.6L$ for the three-sphere and $0.5L$ for the two-capsule constriction. The drop-to-medium viscosity ratio λ is set to 4 for both cases.

The capillary number is defined as

$$\text{Ca} = \frac{\mu_e |\mathbf{u}_\infty| \tilde{a}}{\sigma L}, \quad (2)$$

where μ_e is the external medium viscosity and σ is the constant surface tension of the drop interface S . For the three-sphere constriction and the above parameters, the critical capillary number (below which the drop becomes trapped) was determined to be $\text{Ca}_{\text{crit}} \approx 1$, using the boundary-integral method as discussed at length by Zinchenko and Davis [45]. At the subcritical $\text{Ca} = 0.9$ chosen herein for the three-sphere constriction, the resulting trapped drop is shown in Fig. 1(a) after slowing to a migration velocity of less than $10^{-4}|\mathbf{u}_\infty|$. The solid-particle mesh resolution (total number of triangles comprising the surface) is $\tilde{N}_\Delta = 11\,520$, and the drop resolution is $\tilde{N}_\Delta = 20\,480$. This resolution for the drop is higher than those used by Zinchenko and Davis [45] and was chosen to increase the accuracy of the computed internal velocity field. A plot of drop velocity versus time for a (clean) drop at this resolution prior to trapping is provided by Gissinger *et al.* [48], Fig. 8 therein. For the two-capsule constriction and the above parameters, a capillary number of $\text{Ca} = 0.7$ was

found to be subcritical [46] and chosen for the present study; the corresponding trapped state is shown in Fig. 1(b). Additional simulation details for the three-sphere and two-capsule constrictions are provided in Zinchenko and Davis [45] and Gissinger *et al.* [46].

As a fraction of the vertical distance from the bottommost point of the drop to the topmost, the trapped drop center is at 0.56 for the three-sphere constriction and at 0.52 for the two-capsule case. Notably, the Poincaré sections used herein are defined as the intersection of trajectories with the plane parallel to $(x, y, 0)$ and passing through these drop centers. Here and below, the drop center is understood as the surface centroid:

$$\mathbf{x}_c = \frac{1}{S} \int_S \mathbf{x} dS_x. \quad (3)$$

III. CALCULATION OF THE INTERNAL VELOCITY FIELD

The steady-state droplet configurations used herein were dynamically approached, with high accuracy, using a desingularized boundary-integral algorithm. For both systems, the suite of desingularization methods detailed by Zinchenko and Davis [45] was used, with analytical desingularization integrals replaced by semianalytical integrals in the case of the two-capsule system [46]. The Hebecker representation is used for solid-particle contributions, and the interfacial stress is desingularized for both droplet self-interactions and drop-solid interactions. The result is a system of Fredholm integral equations of the second kind that are well-behaved for tight-squeezing or indefinitely trapped droplets. In the trapped state, there remains a nonzero, although very small (on the order of 1% of L) drop-solid surface clearance due to the flow-induced pumping mechanism [49,50]; this pumping would be absent for gravity-induced trapping.

Once a trapped state is simulated with the interfacial velocity \mathbf{u}_S on the drop surface, the next task is to restore the fluid velocity field inside the drop. The matching viscosities case is much simpler in this respect, since for $\lambda = 1$ the original boundary-integral solution is valid for the entire fluid domain, thus providing the velocity field within the droplet. For a general $\lambda \neq 1$, though, the fluid velocity inside the drop must be recovered from an additional solution of the internal Dirichlet problem for Stokes flow with prescribed boundary values $\mathbf{u} = \mathbf{u}_S$ on S .

Following the general theory [51–54], the flow strictly inside the drop can be sought as a double-layer potential,

$$\mathbf{u}(\mathbf{y}) = 2 \int_S \mathbf{Q}(\mathbf{x}) \cdot \boldsymbol{\tau}(\mathbf{r}) \cdot \mathbf{n}(\mathbf{x}) dS_x, \quad (4)$$

where \mathbf{Q} is an unknown density function. Upon taking the limit $\mathbf{y} \rightarrow S$ and the substitution (Wielandt’s deflation for a container) $\mathbf{Q} = \mathbf{W} - \mathbf{W}'/2$ (where prime indicates rigid-body projection conveniently calculated by the recipe in Zinchenko *et al.* [55]), a fully deflated boundary-integral equation is obtained for \mathbf{W} ,

$$\begin{aligned} \mathbf{W}(\mathbf{y}) = & -2 \int_S \mathbf{W}(\mathbf{x}) \cdot \boldsymbol{\tau}(\mathbf{x} - \mathbf{y}) \cdot \mathbf{n}(\mathbf{x}) dS_x + \mathbf{W}' \\ & - \frac{\mathbf{n}(\mathbf{y})}{S} \int_S \mathbf{W} \cdot \mathbf{n} dS + \mathbf{u}_S(\mathbf{y}) \text{ for } \mathbf{x}, \mathbf{y} \in S, \end{aligned} \quad (5)$$

with the unique solution and the spectral radius less than one, suitable for an iterative solution by the simplest method of successive substitutions.

In numerical implementation, standard desingularization of the double-layer integral in (5) is achieved with the subtraction

$$\begin{aligned} & -2 \int_S \mathbf{W}(\mathbf{x}) \cdot \boldsymbol{\tau}(\mathbf{r}) \cdot \mathbf{n}(\mathbf{x}) dS_x \\ & = -2 \int_S [\mathbf{W}(\mathbf{x}) - \mathbf{W}(\mathbf{y})] \cdot \boldsymbol{\tau}(\mathbf{r}) \cdot \mathbf{n}(\mathbf{x}) dS_x - \mathbf{W}(\mathbf{y}), \end{aligned} \quad (6)$$

valid for $\mathbf{y} \in S$. The tolerance for iterative solution of (5) was set to $10^{-8}|\mathbf{u}_\infty|$. Once \mathbf{W} and \mathbf{Q} are obtained, the internal flow $\mathbf{u}(\mathbf{y})$ is computed using the regularized form of (4),

$$\mathbf{u}(\mathbf{y}) = 2 \int_S [\mathbf{Q}(\mathbf{x}) - \mathbf{Q}(\mathbf{x}^*)] \cdot \boldsymbol{\tau}(\mathbf{r}) \cdot \mathbf{n}(\mathbf{x}) dS_x + 2\mathbf{Q}(\mathbf{x}^*), \quad (7)$$

valid for \mathbf{y} strictly inside S . Here, \mathbf{x}^* is the mesh node on S closest to the observation point \mathbf{y} . Unlike in (6), regularization (7) alleviates but does not completely remove the singular behavior of the double-layer integral, when \mathbf{y} is close to S . The more powerful high-order near-singularity subtraction of Zinchenko and Davis [45] could not be used for Eq. (4) because it would require the droplet to be of a specific shape (sphere, spheroid, or general axisymmetric shape [46]).

IV. VISUALIZATION OF THE INTERNAL VELOCITY FIELD

A. Numerical methods

All reported values are made nondimensional using the far-field velocity and characteristic length of each system.

The velocity and timescales are $|\mathbf{u}_\infty|$ and $L/|\mathbf{u}_\infty|$, respectively. Passive tracers were advected using the fourth-order Runge-Kutta method with a time step of $\Delta t = 1$. Note that the maximum dimensionless velocity within either trapped drop is ≈ 0.01 . Using a time step two orders of magnitude smaller, $\Delta t = 0.01$, with either Runge-Kutta or a simple Euler integration, resulted in visually indistinguishable trajectories, e.g., for the complex orbits discussed in Sec. V. When advecting a material line, a line of tracers, connected in serial by edges of length $l_e = 0.01$, was initialized between two given points, e.g., on the drop interface. When any edge length exceeded l_e , the edge was bisected by adding another tracer. When an edge length dropped below $l_e/2$, its two nodes were merged. When the material line was supposed to lie on a plane of symmetry, all the nodes were projected onto the plane after every time step to correct for numerical drift.

Advection of a material surface closed by an arbitrary boundary, in this case confined to the droplet interface, presented several technical challenges, some of which were unique to using a boundary-integral method for tracer advection. Here, we outline the method at a conceptual level. First, the closed loop that forms the material surface’s boundary was advected by interpolating the interfacial velocity field (alternatively, the boundary-integral problem could be solved for points located on the surface). This loop and the interior material surface were bridged (triangulated) in such a way that interior points did not approach too near to the surface, which would have caused instability due to the singular nature of the boundary-integral formulation. The resolution of the 1D boundary loop was maintained in the same manner as the material line described above and the quality of the entire material surface mesh was also maintained adaptively using a simple edge-length based criteria, similar to that employed by Branicki and Wiggins [39] (see Fig. 6 therein). Edges were bisected (and additional edges and triangles created to maintain a triangulated mesh) if they exceeded $2l_e$ and edge nodes were merged if within $l_e/2$. This simple adaptive mesh scheme does not enforce a limitation on the number of edges per node, but in practice it resulted in a maximum edges per node of about ten. Since there were no per-node quantities to calculate for this passive mesh, there was no technical requirements regarding a minimum or maximum number of first neighbors. Finally, the advected material surface must be visualized, keeping in mind that the aspect of interest is the interaction between the two volumes that it separates within the drop. As shown in Fig. 2, at any given time step, we have a surface that is bounded by the drop interface. The surface is used to carve out two distinct volumes (a feature available in the open source software BLENDER V2.78). These two parts of the drop interior can then be rendered with different colors to mimic translucent dye.

B. Potential sources of error

Studying possibly chaotic dynamical systems numerically is always subject to the degrading effect of round-off errors over long times. However, additional systematic errors can arise when the boundary conditions (herein, the shape and velocity of the drop interface) are also not known analytically. In the present case, e.g., symmetry breaking (see Sec. V, Fig. 8)

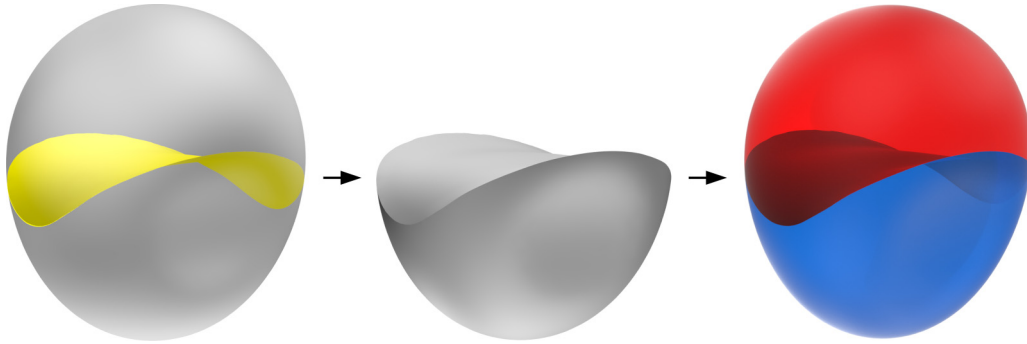


FIG. 2. Summary of how an advecting material surface bounded by the drop interface is visualized. At any given time step, we begin with a material surface (yellow) within a droplet volume (transparent grey). The material surface is used to divide the volume into separate parts (one of which shown in opaque grey). Finally, the two parts can be rendered separately to mimic translucent dyes (red and blue).

can occur, caused by slight offsets of the droplet from the center of symmetric systems, which developed as the droplet approached the particles from its initial upstream position (see Gissinger *et al.* [46] for a discussion of how such effects were mitigated). Additionally, although the boundary-integral equations can be solved with arbitrarily high precision, their singular nature becomes problematic as tracers approach the drop interface. Without refinement of the $\tilde{N}_\Delta = 20$ K resolution droplet meshes used above, small but clearly nonphysical perturbations of trajectories occur within distances of ≈ 0.005 of the interface [using the simple singularity subtraction in Eq. (7)]. These singularity perturbations can have subtle but important effects when calculating dynamics; if tracers always tend to be kicked away from the interface at a given point, apparent periodic orbits can be observed that are, in fact, numerical artifacts rather than representative of the exact system dynamics. For example, an apparent limit cycle in the symmetry plane of the three-sphere droplet could not be adequately resolved due to this issue. It was not uncommon for trajectories to switch between regions separated by symmetry planes. Reducing the time step by two orders of magnitude, $\Delta t = 0.01$, did not reduce or promote this behavior. This basin hopping was likely caused by small numerical asymmetries in the boundary conditions due to the finite drop and solid particle triangulation.

Finally, a boundary integral method was used to obtain these droplet configurations dynamically, and was subject to a convergence tolerance of 1×10^{-5} when solving for interfacial velocities. The trapped state of the droplet is subject to this tolerance as well; in other words, the final droplet velocity is small but nonzero ($\approx 1 \times 10^{-5}$). Therefore, there exists a finite divergence through the interface, i.e., surface integral of the normal component of interfacial velocity, when the interface is assumed to be stationary (for example, divergence is -2.9×10^{-5} for the two-capsule drop). This can cause unphysical behavior of tracers when observed over long enough durations. For example, the apparent KAM torus in Fig. 5(d) spirals slowly inward when observed for durations $> 1 \times 10^5$. The divergence through a sphere of radius 0.03 at the center of this spiral is $\approx 1 \times 10^{-6}$. The overall divergence through the drop surface may be artificially eliminated by subtracting the velocity component orthogonal to the interface. Solving for the internal velocity using this artificial interfacial velocity field significantly decreases the rate of inward trajectory, but

the reported qualitative features of the flow are not affected by this perturbation to the interfacial velocity field.

V. NUMERICAL RESULTS

A. 2D streamlines and equilibria on symmetry planes

Streamlines for the internal velocity field of droplets trapped in three-sphere and two-capsule constrictions are shown in Fig. 3. Planes of symmetry were used to create cutaways of each drop for visualization; a quadrant and a sixth are sliced out of the two-capsule and three-sphere constrictions, respectively. Planes of symmetry are good candidates for equilibria (stagnation points) of the 3D velocity field, and one equilibrium is observed on each of the cutaway faces in Fig. 3 (highlighted with colored dots). The maximum interior dimensionless velocity is ≈ 0.01 and occurs at the drop interface and away from solid-particle surfaces. For both drop-solid configurations, equilibria appear near the lower perimeter of the dimpled near-contact region (formed by lubrication interactions with the solid surface), and near the drop interface. Also, equilibria appear away from the interface in the upper half of each drop. However, these apparently similar pairs of equilibria interact very differently in each of these systems. Not shown are equilibria that exist on the drop interface itself; for example, assuming perfect symmetry, an obvious heteroclinic orbit (trajectory between two different equilibrium points) within both drops is that between the bottommost and the topmost points of each drop, consisting of a simple vertical line along the intersection of the symmetry planes. Small perturbations of a tracer near symmetry planes can greatly affect its long-term dynamics, e.g., by causing it to switch between quadrants of the two-capsule drop.

The equilibria shown in Fig. 3 can be classified by the eigenvalues of the linearized flow. Local linearizations were obtained using a grid centered on the equilibrium with spacing of 0.001 between grid points to calculate velocity gradients by finite differences; using an order of magnitude larger spacing did not affect values within the precision provided in Table I. In all cases, the equilibria have one real eigenvalue and a pair of complex conjugate eigenvalues with a real part of opposite sign. The signs of the eigenvalues confirm that both of the identified equilibria in the three-sphere droplet are 2D unstable and 1D stable; we designate this equilibrium as a (2,1) saddle focus. As can also be deduced from the streamlines

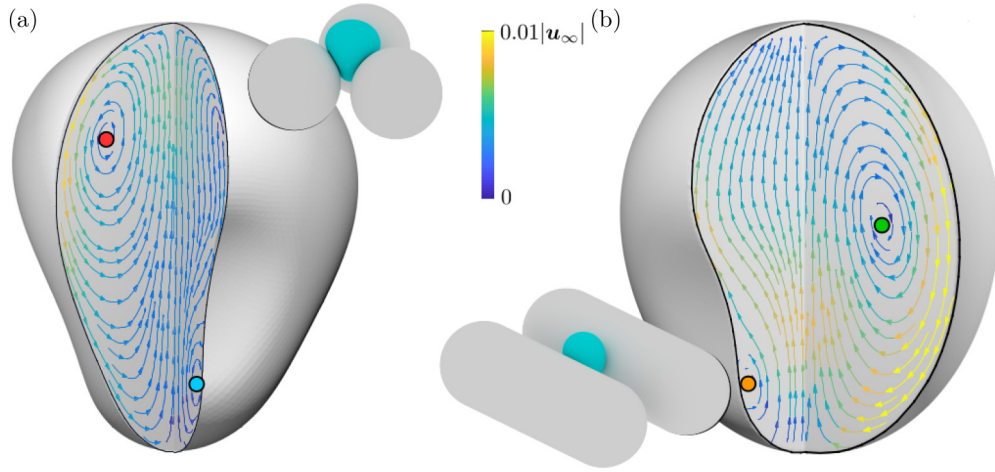


FIG. 3. Cutaways of trapped drops reveal internal dynamics, with velocity magnitude shown in color. (a) A sixth, defined using planes of symmetry, is cut from the three-sphere droplet to reveal two-dimensional streamlines and equilibria (red and blue). (b) A quadrant is cut from the two-capsule droplet, revealing two equilibria (green and orange) on orthogonal symmetry planes.

in Fig. 3, one of the equilibria in the two-capsule is a (1,2) saddle focus. If the system were perfectly symmetric, this equilibrium (green in Fig. 3) would be a sink whose basin of attraction within the drop comprises one-half of its symmetry plane, with the drop centerline as its separatrix. As discussed below, symmetry is broken by numerical artifacts during the dynamic boundary-integral simulation used to create these systems, which destroy the centerline separatrix.





B. Dynamics within the two-capsule droplet

The interactions between the (1,2) and (2,1) saddle foci help define the topological skeleton of the velocity field. The unstable and stable manifolds associated with each type of saddle focus is shown schematically on the right-hand side of Fig. 4(a). On the left-hand side of Fig. 4(a), it can be seen that tracers originating in the two-capsule droplet near the green point flow toward the orange point. One trajectory (bold black curve) is shown that seems to shadow a connection between these saddle foci, but we believe there is not a true heteroclinic orbit between these points (see below). Note that, with a small perturbation of the initial starting point, the tracer could instead flow to the other (2,1) saddle focus, following a mirror-image orbit within another quadrant. To help visualize how this orbit influences the internal flow, the trajectories of 100 tracer particles, all starting in one quadrant but near the drop center, are also shown in color. When observing the time series of tracer trajectories within the two-capsule droplet,

they are most obviously characterized by loops around the near-heteroclinic orbit within a given quadrant. However, attempts to locate a heteroclinic connection between these two equilibria were unsuccessful; instead, the unstable manifold of the (1,2) saddle focus [shown in green and forward time in Fig. 4(b)] nearly misses and is attracted to the unstable manifold of the (2,1) saddle focus (located within a symmetry plane). The stable 1D manifold of the (2,1) saddle focus is shown in red, with the arrow indicating inverted-time flow. Long-time trajectories of these tangled orbits are complex, involving many circulations around the near-heteroclinic orbit. Such trajectories also inevitably approach the drop interface at times, perhaps destroying any hetero- or homoclinic orbits due to the noise of the singular boundary-integral method (highlighting the main drawback of dynamical systems analysis using this formulation). In contrast to this system, both of the equilibria within the three-sphere droplet are (2,1) saddle foci and the internal dynamics are quite different, as discussed below.

The combined Poincaré sections of 100 tracers starting within 0.01 of each other near the center of the two-capsule droplet are shown in black in Fig. 5(a), where 3D trajectories are intersected with the plane parallel to $(x, y, 0)$ and passing through the drop center. The total duration of each trajectory is 5×10^5 , resulting in $>86\,000$ total points of intersection. The points within the blue region result from the one-time flow away from the (1,2) saddle focus, shown in Fig. 5(b) (also shown in Fig. 4). Shortly thereafter, the tracers tend

TABLE I. Eigenvalues of local linearizations of the flow at stagnation points inside the drops.

System	Symbol ^a	Eigenvalues ($\times 10^3$)	Classification
Three-sphere		$(-3.01 + 0.00i, 1.50 + 26.1i, 1.50 - 26.1i)$	(2,1) saddle focus
Three-sphere		$(-2.72 + 0.00i, 1.36 + 18.6i, 1.36 - 18.6i)$	(2,1) saddle focus
Two-capsule		$(-4.12 + 0.00i, 2.06 + 24.7i, 2.06 - 24.7i)$	(2,1) saddle focus
Two-capsule		$(0.41 + 0.00i, -0.20 + 7.46i, -0.20 - 7.46i)$	(1,2) saddle focus

^aSee Fig. 3.

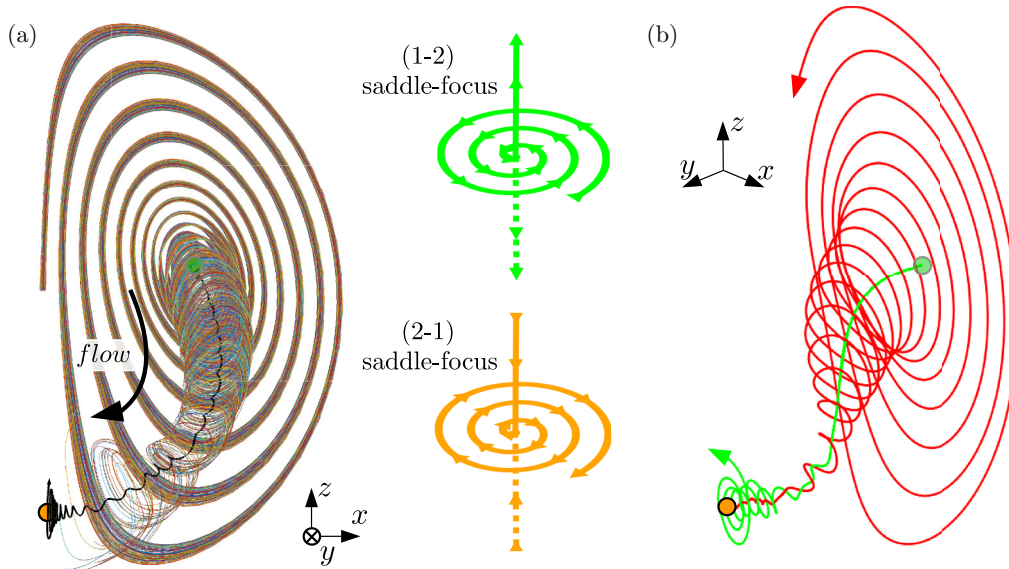


FIG. 4. Internal flow dynamics within a quadrant of the two-capsule droplet revealed by tracers. (a) The interaction between the (1,2) saddle focus (green) and a (2,1) saddle focus (orange) is highlighted by a trajectory (black). In addition, 100 tracers starting near the drop center (placed randomly inside a cube of side length 0.01) are shown in color. See Fig. 3 for location of saddle points with respect to the drop interface. (b) The nonexistence of a heteroclinic orbit between the two saddle foci is shown, with a forward-time trajectory from the green point and reverse-time trajectory from the orange point.

toward regular orbits, as can be inferred from the Poincaré map. One such characteristic orbit is shown in Fig. 5(c), which shows a tracer just before entering the orbit. The orbit is visualized over a total trajectory duration of $>2.5 \times 10^6$, and has a period of ≈ 1125 . It consists of 12 turns but, despite its apparent complexity, is a simple loop (i.e., an unknot, as determined by the method of Dorier *et al.* [56]). Figure 5(a) also reveals a manifold that borders the drop interface. A

tracer initiated in the interior of this manifold, away from its edges, reveals an apparent KAM torus when observed over a duration of 1×10^5 , as shown in Fig. 5(d). As discussed in Sec. IV B, over longer durations this trajectory succumbs to an unphysical inward spiral. The Poincaré section for this orbit over a duration of 1×10^5 is shown, in orange, in Fig. 5(a).

C. Dynamics within the three-sphere droplet

A similar analysis was completed for the three-sphere system, with notably different results. The combined Poincaré section for 100 tracers starting near the droplet center is shown in Fig. 6(a). The stochastic region filling most of the cross section is a classic indicator of chaotic behavior, suggesting enhanced mixing for this threefold-symmetric system as compared to the two-capsule drop. A large prohibited region is also revealed within each sixth of the droplet, which contains more regular orbits. One such trajectory is calculated by randomly placing a tracer within the prohibited region, resulting in five-sided shapes comprising its Poincaré map [shown in Fig. 6(a) in orange]. This relatively stable trajectory is shown in 3D in Fig. 6(b), and revealed to be contained by a torus embedded in the upper part of the droplet, at least within its duration. The shape of the prohibited region and the interior trajectory suggests the existence of islands chains but these could not be located; it is possible that they are destroyed by the divergence or symmetry-breaking issues discussed in Sec. IV B. A trajectory within the large chaotic sea is shown in light blue as it explores much of the surrounding space, including passing through the center of, and around the perimeter of, the stable loop.

For the three-sphere droplet, both of the interior saddle points marked in Fig. 3 are (2,1) saddle foci. Tracers initialized at these points follow chaotic trajectories visually

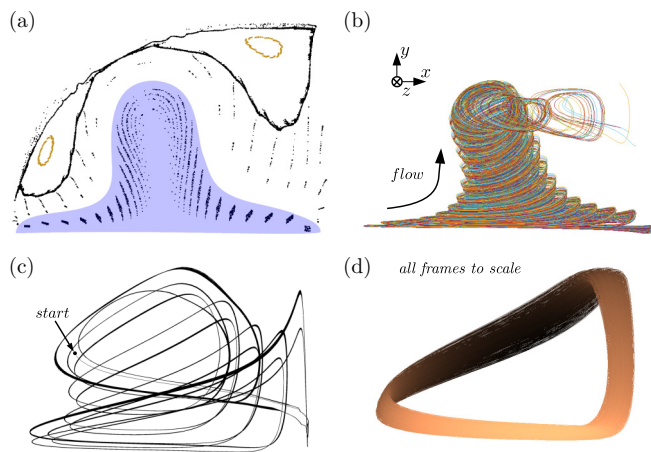


FIG. 5. Visualizations of the flow within a quadrant of the two-capsule drop. Axes in (b) apply to entire figure. (a) The Poincaré section for 100 tracers starting near the droplet center, intersecting with the xy plane that contains the drop center (shown in black). Points within the blue section result from the trajectories shown in (b). A KAM torus is shown in orange. (b) Another view of the trajectories shown in Fig. 4. (c) An example of a complex periodic orbit. (d) The orbit of a single tracer initialized near the center of the manifold in (a). Shaded to emphasize position along the z axis. The Poincaré section of this trajectory is shown in orange in (a).

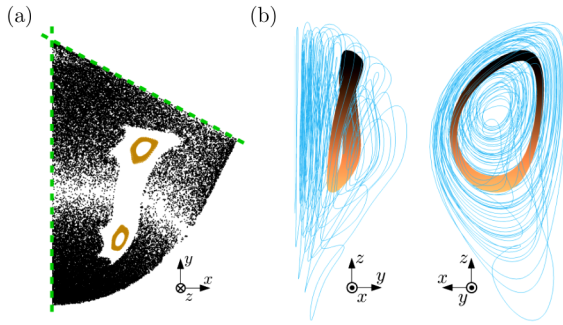


FIG. 6. Dynamic behavior within the three-sphere droplet. (a) Intersections with the xy plane containing the droplet center, for 100 tracers initialized near the droplet center, over a duration of 5×10^5 (shown in black). The Poincaré map of a single tracer initialized outside of the large chaotic sea is also shown in orange, over a trajectory of the same duration. Dotted green lines indicate planes of symmetry. (b) The orbit from frame (b) is shown, colored to indicate position along the z axis. Also shown in light blue is part of a chaotic orbit (over a duration of 2×10^4). Two orthogonal views shown.

similar to that shown in Fig. 6(b). Observations of chaotic tracers show that the saddles interact with each other and themselves. For example, a tracer may flow toward the upper (2,1) saddle focus (the red point in Fig. 3), spiral outward and away from its symmetry plane, and then return, with this pattern repeating a number of times. As shown in Fig. 7, when initializing a tracer at either of these saddles, and letting time run backward, the tracers end up at the top of the drop, after approaching the drop interface. Aside from the top and bottom of the drop, other equilibria on the interface include another point corresponding to a source within the 2D surface, located at the center of the dimpled near-contact region, and a point of extensional flow above the dimple (see Gissinger *et al.* [48], Fig. 10(a) therein, for a visualization of this interfacial field). Based on observing the time series of advected tracers, these features have a less direct influence on the internal dynamics. For example, a tracer starting near the center of dimple, and run backward, first approaches the nearby interior saddle point

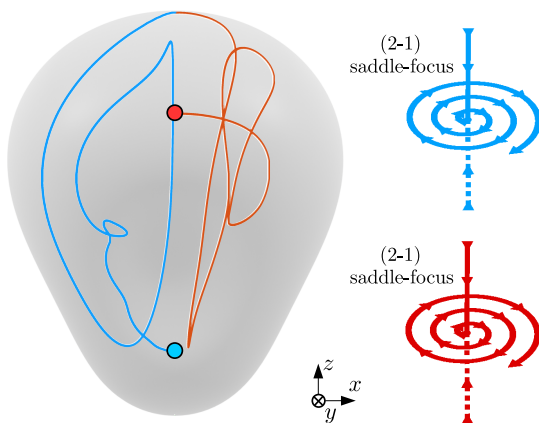


FIG. 7. Reverse-time trajectories from the two (2,1) saddle foci located on one symmetry plane of the three-sphere droplet. In both cases, relatively simple orbits terminate at the stagnation point at the top of the drop, indicating a heteroclinic connection.

before flowing to the top of the drop, resulting in a trajectory similar to those shown in Fig. 7. These backward orbits highlight the important role of the equilibrium at the top of the three-sphere drop, which is repelling along the drop surface and attracting along the drop centerline (in forward time). So, a class of common trajectories can be summarized: A tracer that approaches the centerline and ends up near the top of the drop may flow toward any of the six (2,1) saddle foci, with a small perturbation. In contrast, tracers near the top of the two-capsule droplet are directed along the axial direction of the capsule and seem more likely to shadow the heteroclinic connection between the top and bottom of the drop contained within the drop surface.

D. Mixing within trapped droplets

The 2D flow within the axial symmetry plane of the two-capsule droplet is shown in Fig. 8. Theoretically, all velocity components should lie within the plane but, to remove numerical drift from the velocity of the dye interface, which is calculated in 3D, tracers were projected back on the symmetry plane at each time step. The symmetry breaking between the two counter-rotating vortices is attributed to the drop being slightly offset from the constriction center and would be difficult to prevent for this dynamically created system. The axial cross section shown is almost circular (eccentricity of ≈ 0.27), and so a qualitative similarity to the flow within a sphere or circle is expected. For example, Fig. 8 is analogous to the 2D flow within a circle discussed by Wang *et al.* [27] (see Fig. 6 therein), despite their equations being derived for a very different situation (fully developed flow in a slightly curved pipe). In the present system, the interface is in motion; the filament that forms at the bottom of the droplet becomes arbitrarily thin over time. This embedded 2D field is not divergence-free, as it is a cross section that contains the manifolds of 3D saddle foci; in this case, the unstable 1D manifold of the (1,2) saddle focus induces stretching perpendicular to the plane in Fig. 8, allowing the saddle foci to be attractors within the plane.

The advection of a 2D material surface within the two-capsule drop is shown in Fig. 9. As indicated by the streamlines in Fig. 3, the highest surface velocity occurs midway between the capsules, i.e., in the symmetry plane containing the 2D flow in Fig. 8. The interfacial velocity field pinches the boundary of the material surface toward the circular perimeter and pushes the upper half (red dye) of the drop first outward and downward, then inward and upward. The lack of persistent thin layers between the two dyes is one qualitative indication of relatively poor mixing in the system over this time period. The material surface closely approaches the droplet interface in several locations, especially just above the dimpled near-contact region; selected smoothing of the material surface is done for visualization purposes, as a postprocessing step. Advancing beyond $t \approx 650$ would require additional improvements to the meshing scheme, e.g., curvature-adaptive edge length criteria to resolve the thin filament evolving toward the bottom of the drop.

Advection within the three-sphere droplet is shown in Fig. 10. Upward flow occurs at the center of the drop and more slowly in the near-contact region, and downward flow closer

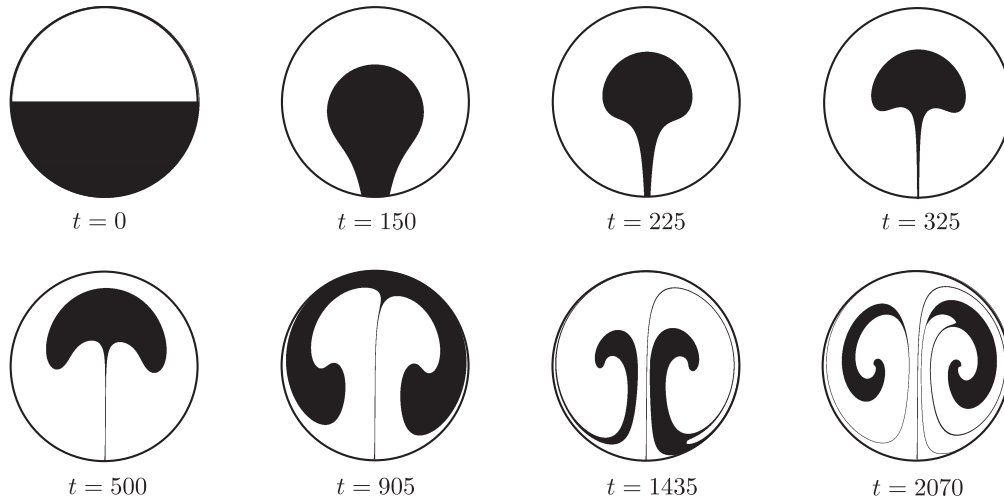


FIG. 8. Advection of a 2D passive dye within the axial symmetry plane of the two-capsule droplet, using the dye interface as a material line. The material line is initialized at the droplet center.

to the interparticle interstices. The material surface quickly increases in complexity, so a cross-sectional cut using one symmetry plane is used for $t > 225$ to reveal the internal dynamics. The development of thin layers between the material surface evidences good mixing, e.g., visible near the center of the drop at $t = 500$. These persistent striations, which do not appear in Fig. 9 over the same timeframe, would allow for quicker diffusion between the two regions in a system with finite Péclet number, especially as thin layers between the material surface accrue. The stretch-and-fold motif, often

cited as a model of chaos, is more obvious for the three-sphere droplet, with stretching of the material surface as it flows toward the top of the drop, and folding (and stretching) as it returns along the interface back toward the bottom. Visual comparison of Figs. 9 and 10 suggests a significantly quicker increase in the surface area and complexity of the interface in the case of the three-sphere droplet; the complexity of the system is quantifiable via topological entropy.

As discussed by Giona and Adrover [57], the growth rates of material lines and surfaces follow the same scaling, i.e.,

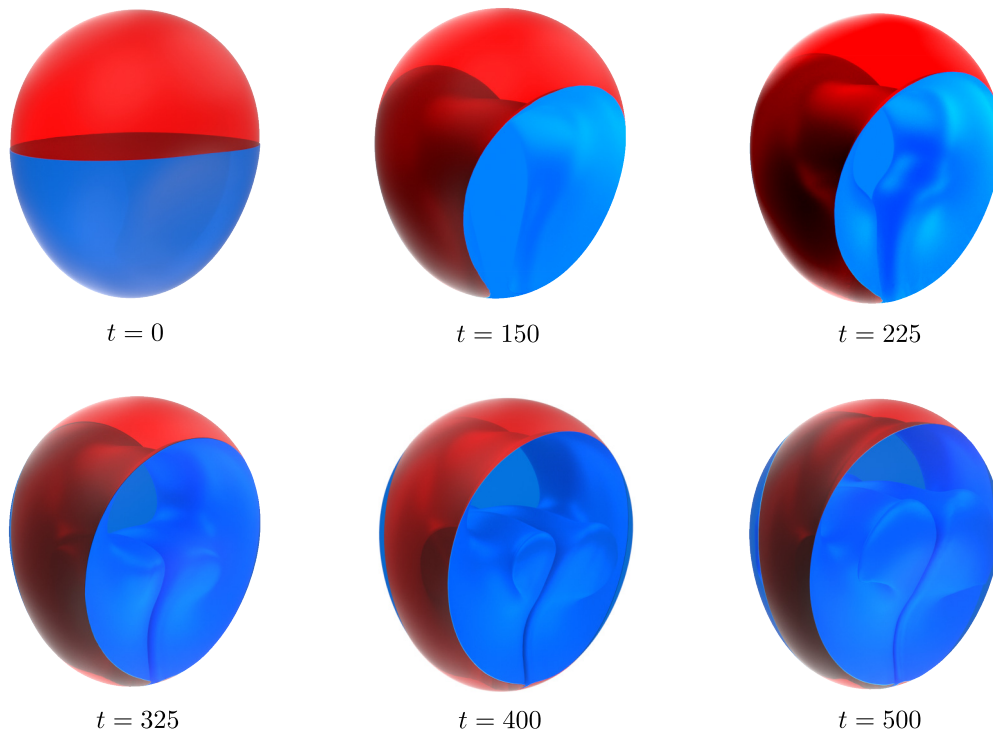


FIG. 9. Advection of a passive material surface within the two-capsule droplet (solid particles hidden). The initial surface lies on the xy plane passing through the drop center. Images are created using the procedure described in Fig. 2, which corresponds to $t = 25$. At $t = 650$, the material surface consists of ≈ 48 K nodes (≈ 95 K triangles).

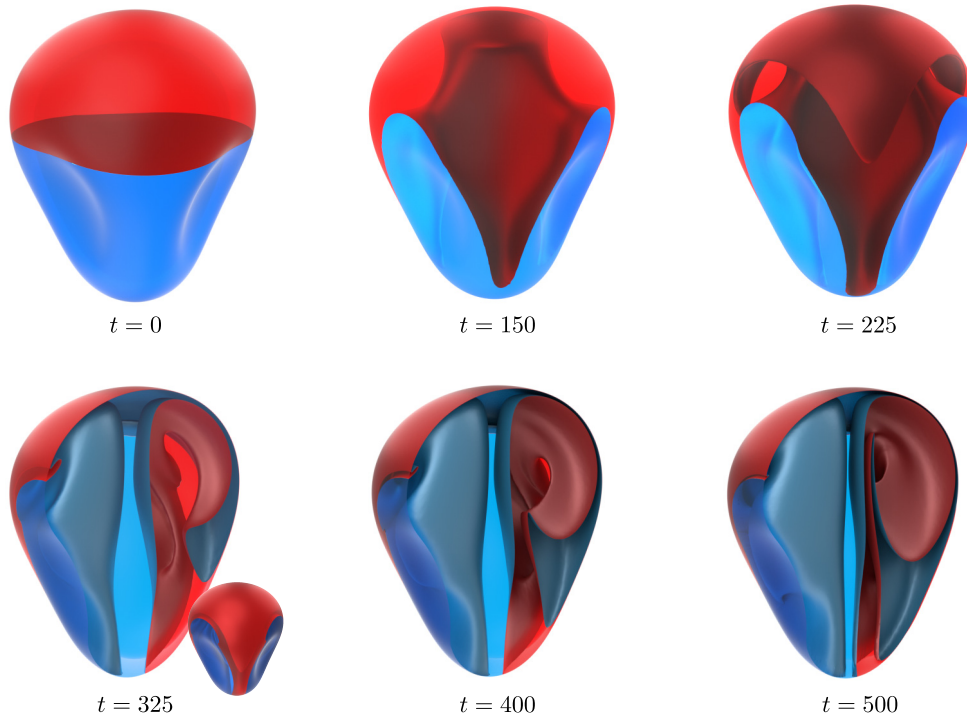


FIG. 10. Advection of a passive material surface separating red and blue dyes within the three-sphere droplet (solid particles hidden), where each face of the material surface is colored according to the dye with which it is in contact. The initial interface lies on the xy plane, passing through the drop center. For $t > 225$, half the droplet is hidden to reveal the internal dynamics (the full droplet is shown as the smaller image at $t = 325$). Visually, this threefold-symmetric system appears considerably more mixing than that of the two-capsule droplet, including the formation of thin layers of each dye by $t = 500$ that could be mixed by diffusion at finite Péclet number. At $t = 500$, the material surface consists of ≈ 150 K nodes (≈ 300 K triangles).

both are related to the topological entropy of the system. So, the relative complexities of the two systems can be quantified by the rate of increase of the material surface area: Over the initial duration of 600, the average rate was 2.7×10^{-2} for the three-sphere droplet and 5.5×10^{-3} for the two-capsule drop. As shown in Fig. 11, the surface area versus time relationship appears to be piecewise linear for $t < 600$. For the three-

sphere droplet, the sharp increase in the rate ($t \approx 160 - 180$) corresponds to the surface initially reaching the top of the drop. If the material surface eventually reaches an exponential growth regime, it is beyond the timescale reachable with our current numerical tools; such a regime could occur when the duration spans many stretch-and-fold cycles associated with the sharp increase in rate of surface area growth.

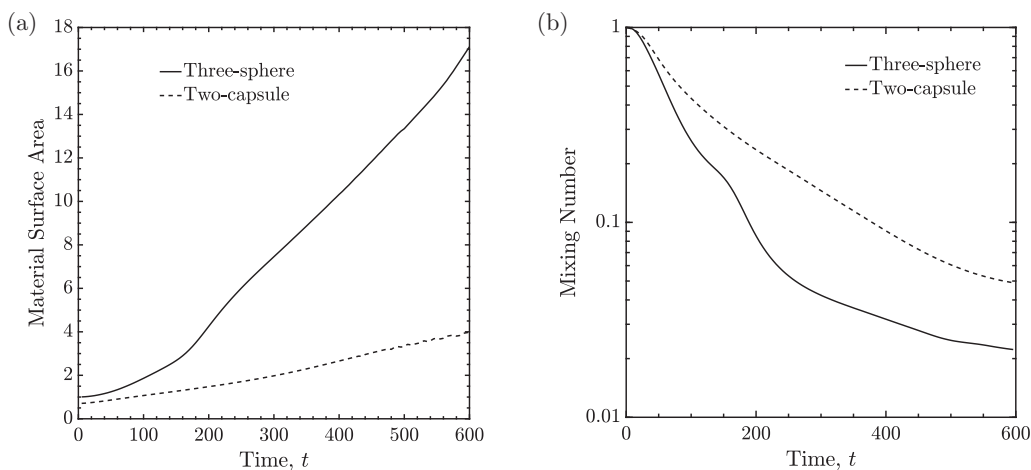


FIG. 11. Mixing metrics for the systems shown in Figs. 9 and 10. (a) Growth of the interfacial area as a function of time. The rate of increase is a measure of system complexity. (b) The mixing number, a measure of how quickly a system can be mixed by diffusion, decays faster for the three-sphere droplet, indicating superior mixing properties.

The 3D mixing within the two systems can be directly quantified using the mixing number proposed by Stone and Stone [43]. This number is the average square distance from each point in the drop to the oppositely colored dye and can provide a direct comparison between systems when normalized by the mixing number at $t = 0$. When the interface between the dyes is well-defined, as by a material surface, this metric equates to the average square distance from the interface. As noted by Stone and Stone [43], the mixing number converges quickly with respect to the number of points sampled within the drop volume. For example, the three-sphere and two-capsule results in Fig. 11(b), respectively, use ≈ 52 K and ≈ 59 K sample points, (chosen using a $50 \times 50 \times 50$ grid and eliminating sample points outside the drop), but the reported values are visually indistinguishable when using only ≈ 3 K sample points. An inverse trend is observed between interfacial area and mixing number, supporting the idea that topological entropy is a good indicator of the system's mixing capability. The faster decay of the mixing number in Fig. 11(b) for the three-sphere drop quantifies its superior mixing qualities over the two-capsule drop. The two-capsule drop reaches $\approx 5\%$ of its original mixing number, while the three-sphere drop falls to less than half that ($\approx 2\%$).

VI. CONCLUDING REMARKS

The internal flows of deformable droplets after reaching the steady state within two types of passive droplet traps, modeled by three-sphere and two-capsule constrictions, are examined. The systems were previously created using the boundary-integral method, for which initial velocity data are available solely at the drop interface. In the present paper, the interior velocity fields were recovered by solving the internal Dirichlet problem, also with a (partially) desingularized boundary-integral method using the double-layer formulation. Standard tools from dynamical systems theory, such as integral curves and Poincaré maps, are utilized to reveal the topological structure and properties of each system. Nondiffusive mixing within each droplet is visualized and quantified by advection of linked tracer particles. For example, in 2D, the material line that bounds two passive dyes is explicitly tracked using an adaptive number of tracers. In 3D, a procedure is introduced for advecting material surfaces bounded by arbitrary, time-dependent closed curves, and this 3D contour advection is used to visualize both chaotic and regular mixing within droplets.

Interior equilibria on the symmetry planes of each flow are identified to be saddle foci. In both cases, two interior saddle points are located on each symmetry plane, with one saddle point in the upper half of the droplet and the second

one just below the dimpled region nearly coating the solid particles. However, these apparently similar configurations give rise to very different flow dynamics. For the two-capsule droplet, the upper saddle point is a (1,2) saddle focus, and the lower is a (2,1) saddle focus. The interaction between these equilibria influences the flow dynamics, which include complex but regular orbits. The analogous equilibria within the three-sphere droplet are both (2,1) saddle foci. A Poincaré section at the center of the three-sphere droplet, created by tracers starting near the drop center, reveals chaotic behavior throughout most of the droplet. Finally, the mixing within both droplets is visualized using material lines and surfaces, which bound two passive dyes, each initially filling one-half of the drop. Qualitative observations suggest that the three-sphere system has greater tendency to create finely striated layers between the dyes. The higher rate of growth of the material surface and faster decay of the mixing number within the three-sphere droplet versus the two-capsule droplet reinforces the conclusion that the three-sphere configuration results in a more effective droplet mixer.

Confined, deformable droplets swept along by a carrier fluid are a common occurrence in the physical world. The juxtaposition between this easily realizable, and comprehensible, system and its complex dynamics makes for an interesting study and its analysis is only limited by dynamical systems theory and related fields. For example, slightly more advanced classifications of the interior flow could include identification of all elliptic, hyperbolic, etc. points, as well as calculation of Lyapunov exponents. Several direct extensions of the current work are also possible. All techniques used herein can be applied to transient drops, e.g., undergoing periodic motion. More experimentally practical systems could include droplets within channels. Due to the highly sensitive nature of chaotic trajectories and their tendency to approach the drop interface, future studies of mixing in deformable droplets should consider more advanced desingularization or interpolation techniques, such as quadrature by expansion [58]. Also, a curvature-adaptive mesh resolution would be helpful, allowing for the resolution of arbitrarily thin 3D filaments while also decreasing the computational requirements of low-curvature regions of the material surface.

ACKNOWLEDGMENTS

The authors gratefully acknowledge helpful correspondence with Saverio E. Spagnolie and James D. Meiss, as well as beneficial suggestions from two anonymous referees. J.R.G. was supported by a fellowship from the U.S. Department of Education Graduate Assistance in Areas of National Need (GAANN) Program (Contract No. P200A180070).

- [1] A. Huebner, D. Bratton, G. Whyte, M. Yang, A. J. deMello, C. Abell, and F. Hollfelder, *Lab Chip* **9**, 692 (2009).
- [2] J. M. Ottino, *Annu. Rev. Fluid Mech.* **22**, 207 (1990).
- [3] H. Aref, J. R. Blake, M. Budisic, S. S. S. Cardoso, J. H. E. Cartwright, H. J. H. Clercx, K. ElOmari, U. Feudel, R.

- Golestanian, E. Guillard, Gert Jan F. van Heijst, T. S. Krasnopolskaya, Y. LeGuer, R. S. MacKay, V. V. Meleshko, G. Metcalfe, I. Mezic, A. P. S. deMoura, O. Piro, M. F. M. Speetjens, R. Sturman, J. L. Thiffeault, and I. Tuval, *Rev. Mod. Phys.* **89**, 025007 (2017).

- [4] H. Aref, *J. Fluid Mech.* **143**, 1 (1984).
- [5] H. Aref, T. A. Dunaeva, and V. V. Meleshko, *Int. J. Fluid Mech. Res.* **29**, 525 (2002).
- [6] V. I. Arnold, *C. R. Acad. Sci. Paris* **261**, 17 (1965).
- [7] T. Dombre, U. Frisch, J. M. Greene, M. Hénon, A. Mehr, and A. M. Soward, *J. Fluid Mech.* **167**, 353 (1986).
- [8] P. S. Contreras, I. Ataei-Dadavi, M. F. M. Speetjens, C. R. Kleijn, M. J. Tummers, and H. J. H. Clercx, *Phys. Fluids* **31**, 123601 (2019).
- [9] K. Bajer and H. K. Moffatt, *J. Fluid Mech.* **212**, 337 (1990).
- [10] H. A. Stone, A. Nadim, and S. H. Strogatz, *J. Fluid Mech.* **232**, 629 (1991).
- [11] H. Stone, A. Stroock, and A. Ajdari, *Annu. Rev. Fluid Mech.* **36**, 381 (2004).
- [12] G. Boffetta, G. Lacorata, G. Redaelli, and A. Vulpiani, *Physica D: Nonlinear Phenom.* **159**, 58 (2001).
- [13] S. Wiggins and J. M. Ottino, *Philos. Trans. R. Soc. London. Series A: Math. Phys. Eng. Sci.* **362**, 937 (2004).
- [14] R. Forman, *Séminaire Lotharingien de Combinatoire* **48**, 35 (2002).
- [15] T. Weinkauff, Ph.D. thesis, University Magdeburg, 2008.
- [16] M. Madadelahi and A. Shamloo, *Int. J. Multiphase Flow* **97**, 186 (2017).
- [17] P. Abbyad, R. Dangla, A. Alexandrou, and C. N. Baroud, *Lab on a Chip* **11**, 813 (2011).
- [18] S. C. Jana, G. Metcalfe, and J. M. Ottino, *J. Fluid Mech.* **269**, 199 (1994).
- [19] M. R. Bringer, C. J. Gerdt, H. Song, J. D. Tice, and R. F. Ismagilov, *Philos. Trans. Series A* **362**, 1087 (2004).
- [20] H. Song and R. F. Ismagilov, *J. Am. Chem. Soc.* **125**, 14613 (2003).
- [21] M. Oishi, H. Kinoshita, T. Fujii, and M. Oshima, *Meas. Sci. Technol.* **22**, 105401 (2011).
- [22] Z. Liu, M. Li, Y. Pang, L. Zhang, Y. Ren, and J. Wang, *Phys. Fluids* **31**, 022004 (2019).
- [23] J. Znaien, M. F. M. Speetjens, R. R. Trieling, and H. J. H. Clercx, *Phys. Rev. E* **85**, 066320 (2012).
- [24] X. Xu and G. M. Homsy, *Phys. Fluids* **19**, 013102 (2007).
- [25] M. F. M. Speetjens, H. J. H. Clercx, and G. J. F. V. Heijst, *J. Fluid Mech.* **514**, 77 (2004).
- [26] E. S. Szalai, M. M. Alvarez, and F. J. Muzzio, in *Handbook of Industrial Mixing* (John Wiley & Sons, Inc., Hoboken, NJ, 2004), pp. 89–143.
- [27] L. Wang, Y. Fan, and Y. Chen, *Int. J. Bifurcation Chaos* **11**, 1953 (2001).
- [28] N. J. Zabusky, M. H. Hughes, and K. V. Roberts, *J. Comput. Phys.* **30**, 96 (1979).
- [29] D. G. Dritschel, *J. Comput. Phys.* **77**, 240 (1988).
- [30] D. W. Waugh and R. A. Plumb, *J. Atmos. Sci.* **51**, 530 (1994).
- [31] J. G. Franjione and J. M. Ottino, *Phys. Fluids* **30**, 3641 (1987).
- [32] S. C. Jana, M. Tjahjadi, and J. M. Ottino, *AIChE J.* **40**, 1769 (1994).
- [33] J. C. H. Fung and J. C. Vassilicos, *Phys. Fluids A: Fluid Dyn.* **3**, 2725 (1991).
- [34] B. A. Mosovsky and J. D. Meiss, *SIAM J. Appl. Dyn. Syst.* **11**, 1785 (2012).
- [35] J.-L. Thiffeault, *Physica D: Nonlinear Phenom.* **198**, 169 (2004).
- [36] S. Candelaresi, D. I. Pontin, and G. Hornig, *Chaos: Int. J. Nonlinear Sci.* **27**, 093102 (2017).
- [37] P. L. Boyland, H. Aref, and M. A. Stremler, *J. Fluid Mech.* **403**, 277 (2000).
- [38] J.-L. Thiffeault and M. D. Finn, *Philos. Trans. R. Society A* **364**, 3251 (2006).
- [39] M. Branicki and S. Wiggins, *Physica D: Nonlinear Phenom.* **238**, 1625 (2009).
- [40] G. Haller, *Annu. Rev. Fluid Mech.* **47**, 137 (2015).
- [41] M. Liu, F. J. Muzzio, and R. L. Peskin, *Chaos, Solitons Fractals* **4**, 869 (1994).
- [42] C. A. Florek and C. L. Tucker, *Phys. Fluids* **17**, 053101 (2005).
- [43] Z. B. Stone and H. A. Stone, *Phys. Fluids* **17**, 063103 (2005).
- [44] M. Finn, S. Cox, and H. Byrne, *J. Eng. Math.* **48**, 129 (2004).
- [45] A. Z. Zinchenko and R. H. Davis, *J. Fluid Mech.* **564**, 227 (2006).
- [46] J. R. Gissinger, A. Z. Zinchenko, and R. H. Davis, *J. Fluid Mech.* **908**, A33 (2021).
- [47] A. Z. Zinchenko and R. H. Davis, *J. Fluid Mech.* **725**, 611 (2013).
- [48] J. R. Gissinger, A. Z. Zinchenko, and R. H. Davis, *J. Fluid Mech.* **878**, 324 (2019).
- [49] M. B. Nemer, Ph.D. thesis, Yale University, 2003.
- [50] M. B. Nemer, X. Chen, D. H. Papadopoulos, J. Bławdziewicz, and M. Loewenberg, *Phys. Rev. Lett.* **92**, 114501 (2004).
- [51] C. Pozrikidis, *Boundary Integral and Singularity Methods for Linearized Viscous Flow* (Cambridge University Press, Cambridge, UK, 1992).
- [52] H. Power and L. C. Wrobel, *Boundary Integral Methods in Fluid Mechanics* (Computational Mechanics Publications, Southampton, UK, 1995).
- [53] C. A. Brebbia, J. C. F. Telles, and L. C. Wrobel, *Boundary Element Techniques: Theory and Applications in Engineering* (Springer Science & Business Media, Berlin, Germany, 2012).
- [54] S. Kim and S. J. Karrila, *Microhydrodynamics: Principles and Selected Applications* (Courier Corporation, North Chelmsford, MA, 2013).
- [55] A. Z. Zinchenko, M. A. Rother, and R. H. Davis, *Phys. Fluids* **9**, 1493 (1997).
- [56] J. Dorier, D. Goundaroulis, F. Benedetti, and A. Stasiak, *Bioinformatics (Oxford, England)* **34**, 3402 (2018).
- [57] M. Giona and A. Adrover, *Phys. Fluids* **13**, 1254 (2001).
- [58] L. af Klinteberg and A.-K. Tornberg, *J. Comput. Phys.* **326**, 420 (2016).